LAWRENCE
LIVERMORE
NATIONAL
LABORATORY

UCRL-JRNL-236685

Upper mantle structure under western Saudi Arabia from Rayleigh wave tomography and the origin of Cenozoic uplift and volcanism on the Arabian Shield

Y. Park, A. Nyblade, A. Rodgers, A. Al-Amri

November 20, 2007

Geochemistry, Geophysics, Geosystems

Disclaimer

Upper mantle structure under western Saudi Arabia from Rayleigh wave tomography and the origin of Cenozoic uplift and volcanism on the Arabian Shield

Yongcheol Park and Andrew A. Nyblade

Department of Geosciences, Penn State University, University Park, PA 16802

Arthur J. Rodgers

Lawrence Livermore National Laboratory, Geophysics and Global Security Division, PO Box 808, Livermore, CA 94551-9900, USA.

Abdullah Al-Amri

King Saud University, Geophysical Observatory, Riyadh, Kingdom of Saudi Arabia

Submitted to G-Cubed on Nov. 14, 2007

Abstract

The shear velocity structure of the shallow upper mantle beneath the Arabian Shield has been modeled by inverting new Rayleigh wave phase velocity measurements between 45 and 140 s together with previously published Rayleigh wave group velocity measurement between 10 and 45 s. For measuring phase velocities, we applied a modified array method that minimizes the distortion of raypaths by lateral heterogeneity. The new shear velocity model shows a broad low velocity region in the lithospheric mantle across the Shield and a low velocity region at depths ≥ 150 km localized along the Red Sea coast

and Makkah-Madinah-Nafud (MMN) volcanic line. The velocity reduction in the upper mantle corresponds to a temperature anomaly of ~250 – 330 K. These finding, in particular the region of continuous low velocities along the Red Sea and MMN volcanic line, do not support interpretations for the origin of the Cenozoic plateau uplift and volcanism on the Shield invoking two separate plumes. When combined with images of the 410 and 660 km discontinuities beneath the southern part of the Arabian Shield, body wave tomographic models, a S-wave polarization analysis, and SKS splitting results, our new model supports an interpretation invoking a thermal upwelling of warm mantle rock originating in the lower mantle under Africa that crosses through the transition zone beneath Ethiopia and moves to the north and northwest under the eastern margin of the Red Sea and the Arabian Shield. In this interpretation, the difference in mean elevation between the Platform and Shield can be attributed to isostatic uplift caused by heating of the lithospheric mantle under the Shield, with significantly higher region along the Red Sea possibly resulting from a combination of lithosphere thinning and dynamic uplift.

1.0 Introduction

The Arabian Shield, with a mean elevation of ~1.2 km and consisting of Neoproterozoic accreted island arc terrains capped in several places by Tertiary and Quaternary volcanic fields, was part of the Nubian Shield until c. 30 – 35 Ma when Arabia rifted from Africa [*Martinez and Cochran*, 1988]. The Cenozoic uplift and volcanism on the Shield have been commonly attributed to hot upper mantle under the Shield [e.g., *Almond*, 1986; *Berhe*, 1997; *Bohannon*, 1989; *Bohannon et al.*, 1989; *Camp and Roobol*, 1989; *Coleman and McGuire*, 1988; *Gettings and Anonymous*, 1981; *McGuire*, 1988; *McGuire and Bohannon*, 1989; *Zeyen et al.*, 1997], but the nature of the upper mantle thermal anomaly remains largely unknown.

To investigate further the geodynamic origin of this anomaly, here we model the seismic shear wave velocity structure of the shallow upper mantle beneath the Arabian Shield by inverting Rayleigh wave phase velocity measurements between 45 and 140 s together with previously published Rayleigh wave group velocity measurements between 10 and 45 s from Pasyanos [2005]. The Rayleigh wave phase velocity measurements between 45 and 140 s have been made using teleseismic earthquake data mainly from the Saudi Arabia National Digital Seismic Network (SANDSN) [*Al-Amri and Al-Amri*, 1999]. Model results provide improved constrains on the spatial extent of the upper mantle thermal

anomaly and associated rock temperatures, yielding new insights about how the thermal anomaly may have formed.

In a companion study, Park et al. [2007], using P- and S-wave body wave travel time tomography, obtained velocity models of upper mantle structure between depths of 150 and 400 km. Structure above 150 km depth could not be well resolved [*Park et al.*, 2007], and, in addition, beneath the middle part of the Arabian Shield, Park and co-workers could not image mantle structure at any depth because of limited ray coverage resulting from the large spacing of seismic stations in the central part of the Shield. This study compliments the work of Park et al. [2007] in that the shear wave velocity structure to a depth of 200 km has been imaged beneath the entire Arabian Shield.

2.0 Background

Although much of the uplift on the Arabian Shield happened between 20 – 13 Ma [*McGuire and Bohannon*, 1989], the magmatism on the Arabian shield occurred in different stages. Camp and Roobol [1992] suggested two stages based on radiometric ages taken from several studies [e.g., *Camp and Roobol*, 1989; *Camp et al.*, 1991; *Capaldi et al.*, 1987; *Civetta et al.*, 1978; *Coleman and McGuire*, 1988; *du Bray et al.*, 1991; *Pallister*, 1987;

Sebai et al., 1991]. The older magmatic stage, between 30 and 20 Ma, is generally associated with the flood basalts in Yemen and Ethiopia [*Civetta et al.*, 1978; *Mohr*, 1983; *Mohr et al.*, 1988]. The younger magmatic event, which commenced at 12 Ma and continues to the present day, formed the N-S oriented Makkah-Madinah-Nafud (MMN) volcanic line (Rahat, Khayba and Ithnayn Harrats in Figure 1)[*Camp and Roobol*, 1992]. As mentioned in the introduction, the uplift and volcanism are generally thought to be the result of hot, buoyant material in the upper mantle associated with a shallow lithosphere-asthenosphere boundary.

The upper mantle structure of the Arabian Plate has been investigated in many studies using a variety of seismic techniques. Most studies find lower-than-average upper mantle seismic velocities beneath the Shield, consistent with the presence of a broad thermal anomaly. Some global tomographic studies suggest that the low velocity anomaly could extend from shallow upper mantle depths downward across the transition zone and into the lower mantle [e.g., *Grand*, 2002; *Montelli et al.*, 2006; *Ritsema et al.*, 1999; *Zhao*, 2001]. Continental-scale tomographic models also show a broad low velocity zone beneath the Arabian Shield that extends into the transition zone and possibly deeper [*Debayle et al.*, 2001; *Pasyanos and Walter*, 2002; *Villaseñor et al.*, 2001]. However, receiver function

studies of the 410 and 660 km discontinuities report little evidence for thermally perturbed mantle transition zone structure beneath the Shield [*Benoit et al.*, 2003; *Kumar et al.*, 2002].

In regional-scale studies, several modeling approaches have been used to constrain shallow upper mantle structure beneath the Arabian Shield. Pn [*Al-Damegh et al.*, 2004; *Al-Lazki et al.*, 2004; *Mellors et al.*, 1999] and Sn tomography models [*Al-Damegh et al.*, 2004; *Sandvol et al.*, 2001] suggest a broad region of inefficient wave propagation under the Shield that is consistent with uppermost mantle P- and S-wave velocities of 7.9 and 4.3 km/s, respectively obtained by modeling regional waveforms [*Rodgers et al.*, 1999] and receiver functions [*Julia et al.*, 2003; *Kumar et al.*, 2002; *Tkalčić et al.*, 2006], as well as with results from body and surface wave tomography models [*Benoit et al.*, 2003; *Maggi and Priestley*, 2005; *Park et al.*, 2007].

Thermally perturbed upper mantle is also indicated by shear wave splitting results, which show a pattern of N-S fast polarization directions for SKS waves across the Shield [*Hansen et al.*, 2006; *Wolfe et al.*, 1999]. Hansen et al. [2006] attributed the pattern to a combination of plate and density driven flow in the asthenosphere, with the density driven flow coming from warm material flowing to the northwest from the Afar hotspot channeled

by thinner lithosphere under the Red Sea and the western edge of the Shield. This interpretation is supported by a recent analysis of S wave receiver functions that suggests thinner (~70 km thick) lithosphere under the western side of the Shield and thicker (~100 – 150 km thick) lithosphere under the rest of the Shield and Platform [*Hansen et al.*, 2007].

3.0 Data and phase velocity measurements

3.1 Seismic stations and earthquake data

Teleseismic earthquake data used in this study were obtained primarily from the Saudi Arabia National Digital Seismic Network (SANDSN). The SANDSN has been operated since 1998 by the King Abdulaziz City for Science and Technology (KACST) [*Al-Amri and Al-Amri*, 1999]. The network consists of thirty-eight stations unevenly spaced across western Saudi Arabia, twenty-seven of which are equipped with broadband (Streckeisen STS-2) seismometers (Figure 1). Five years of data (1999-2003) from twenty-two of the broadband stations were made available for this study.

In order to increase ray coverage, we augmented the SANDSN data with other available data, including data from the Saudi Arabia PASSCAL Experiment, the Ethiopia Broadband Seismic Experiment, and the IRIS/GEOSCOPE permanent seismic stations,

ATD, EIL, MRNI, and RAYN (Figure 1). The Saudi Arabia PASSCAL Experiment consisted of nine broadband seismic stations deployed for 18 months between late 1995 and early 1997 [*Vernon et al.*, 1996], while the Ethiopia Broadband Seismic Experiment consisted of 27 broadband stations operated between 2000 and 2002 [*Nyblade and Langston*, 2002]. From these data sets we selected 180 teleseismic events with Ms greater than 5.8 between distances of 30° and 150°. The azimuthal distribution of events is reasonably good, although the majority of the events come from back-azimuth ranges between 15 to 130 and 230 to 290 degrees (Figure 2).

3.2 Phase velocity measurements

All waveforms were visually inspected and the selected high-quality ones were corrected by removing the instrument response and trend, and then resampled at 2 samples per second. Cross correlelograms were computed from all pairs of vertical component displacement seismograms, which were then filtered in 30 period bands ranging from 16 to 180 s using the multiple filter technique (MFT) [*Dziewonski et al.*, 1969] with the Gaussian Filter Algorithm [*Shim*, 1989]. In this method, the width of each Gaussian band-pass filter is narrowed by $1/t_c$ (t_c: the central period for each band-pass width). The differential travel

time (Δt_{ij}) of the Rayleigh wave was then computed from the filtered correlograms for pairs of stations i and j at each period.

The incoming wavefront and the azimuth of propagation for teleseismic surface waves can be distorted by lateral heterogeneity between the source and the array. To measure the true azimuth, Menke and Levin [2002] introduced an array method with three or more differential travel times. The differential travel-time is represented by $\Delta t_{ij} = p(\omega)\Delta x_{ij}$, where $p(\omega)$ is the phase slowness, and Δx_{ij} is great circle distance ($r_j - r_i$) between the hypocenter and station i (r_i) and j (r_j), respectively. Menke and Levin [2002] solved for the two unknown components of the phase slowness, p_x and p_y, in Cartesian coordinates. Lawrence et al. [2006] modified this method for a spherical wavefront reference frame, in which the slowness is given by $p = [\Delta x^T \Delta x]^{-1} \Delta x^T \Delta t$. This equation can be solved for the slowness vector for the tangential (p_T) and radial (p_R) axes of the spherical wavefront reference frame by replacing the orthogonal distances (Δx_{ij}) with the radial distance (ΔR_{ij}) along the ray path from event to station and the tangential distance (ΔT_{ij}) along the wavefront. The radial and tangential distances are obtained from

$$\begin{bmatrix} \Delta R_{ij} \\ \Delta T_{ij} \end{bmatrix} = \begin{bmatrix} \cos(baz_j - baz_{ij}) \\ \sin(baz_j - baz_{ij}) \end{bmatrix} d_{ij},$$

where baz_i is the azimuth between station i and the event, baz_{ij} is the inter-station angle between stations i and j, and d_{ij} is the inter-station distance. The back azimuth correction (θ) is computed by $\theta = \tan^{-1}(p_T / p_R)$.

In this study, we applied the modified array method by Lawrence et al. [2006] to minimize the distortion of raypaths introduced by using Cartesian coordinates. After correcting the back azimuth for each period, we removed outliers defined as 1) measurements at a particular period that greatly differed from phase velocities ($\delta \ln c > 10\%$) for contiguous periods, and 2) rays having a deviation of azimuth between station-to-station and station-to-event greater than 20°. Ray coverage varies with each period because of decreasing signal-to-noise ratio at long periods, multi-path interference, and rapid changes in velocity at shorter periods. We obtained a maximum number of 1606 rays at 70 s period, and more than 1200 rays for each period between 45 and 140 s (see selected ray path maps in Figure 3). For further analyses, therefore, we used only the phase velocity measurements between periods of 45 s to 140 s.

3.3 Inversion results for 2D phase velocity maps

Two-dimensional phase velocity maps for each period were generated by inverting the dispersion measurements using the LSQR algorithm [*Paige and Saunders*, 1982] with a 50 km × 50 km grid of cells. During the inversion procedure, a Laplacian smoothing technique was applied, and optimum smoothing parameters were selected through an investigation of trade-off curves of Rayleigh wave phase travel-time misfit vs. a Laplacian measure of two-dimensional model roughness. The trade-off curves for all period bands are similar. A representative curve is shown in Figure 4. Model uncertainties for each phase velocity map were estimated using a bootstrap resampling technique [*Shim*, 1989], 200 iterative inversions and three quarters of the total number of rays available for each period. The highest uncertainty (~0.06 km/s) was obtained in the southern part of the Arabian Shield.

For examining model resolution, we conducted resolution tests with synthetic checkerboard models at all periods. Figure 5 shows results for periods of 52 s, 80 s, 100 s, and 140 s. The synthetic phase velocity and raypaths for the Rayleigh waves were computed for a 300 km × 300 km checkerboard consisting of fast and slow velocity anomalies of ±10%. The input checkerboard outlines are shown on each recovered model with gray lines (Figure 5). Since a smoothing technique was applied during the inversion,

the checkerboard tests cannot resolve the sharp boundaries. From the retrieved maps it can be seen that away from the cell boundaries the shape of the input model is well recovered at all periods in the middle part of the Shield. In contrast, input checkers in the southern part of the Shield are smeared in a northeasterly direction for higher period bands, while checkers in the northern part of the Shield smear in a northwesterly direction, consistent with the ray coverage in Figure 3.

Figure 6 shows the phase velocity maps for selected periods. Based on the checkerboard resolution tests (Figure 5), the region that can be best resolved is surrounded by a bold white polygon. At all periods, a low velocity anomaly (~ -5%) is observed under the MMN volcanic line, and an even larger low velocity anomaly (~ -8%) is seen beneath the southern part of the Shield.

4.0 Inversion for mantle structure

4.1 Initial model setup for each inversion point

To obtain an image of the shear velocity structure of the crust and upper mantle, we inverted for a one dimensional velocity profile for each point in the region shown in Figure 6 using our Rayleigh wave phase velocities from 45 to 140 s period and Rayleigh wave

group velocities between 10 and 45 s period from Pasyanos [2005]. Velocity models obtained from inverting dispersion curves do not generally resolve sharp boundaries very well, such as the Moho discontinuity, because surface waves have broad depth sensitivities at each period. Thus, in the inversion we constrained crustal thickness using a model of Moho depths based on receiver function studies [*Al-Damegh et al.*, 2005; *Kumar et al.*, 2002] and seismic refraction profiles [*Mooney et al.*, 1985]. Figure 7a shows our model obtained by taking the results from Al-Damegh et al. [2005], Kumar et al. [2002], and Mooney et al. [1985], and interpolating between them using a minimum curvature gridding algorithm [*Smith and Wessel*, 1990]. For comparison, in Figure 7b we shows Moho depths from the CRUST2.0 model [*Bassin et al.*, 2000]. There are a few differences between the two models. The CRUST2.0 model shows Moho depths greater than 40 km on the northern edge of the Shield, where crustal models obtained by analyzing receiver functions show Moho depths of less than 40 km. Other differences include shallower Moho depths (< 25 km vs. 33 km) along the middle portion of the Red Sea coast and deeper depths (40 km vs. < 25 km) along the southern part of the Red Sea coast.

The starting one-dimensional crustal model for each point included a Moho depth taken from Figure 7a. Four-layer and five-layer crustal models were used for points in the

Shield and Platform, respectively, with velocities for each layer taken from CRUST2.0. For structure below the Moho, the isotropic PREM model [*Dziewonski et al.*, 1981] was used, but with an Sn velocity of 4.3 km/s for points in the Arabian Shield, which is the Sn velocity reported in many regional studies [e.g., *Julia et al.*, 2003; *Knox et al.*, 1998; *Rodgers et al.*, 1999]. Each 1D model for the Shield consisted of 23 layers, while 24 layers were used for the Platform. The thickness of each layer between Moho and 110 km depth was 10 km, and 20 km below a depth of 110 km. To constrain the Moho depth in the inversion the first layer below the Moho was heavily weighted so that the Moho depth and Sn velocity obtained from the inversion would not differ significantly from the starting model. For example, the average Sn velocity obtained from the inversion is 4.35 km/s.

The one-dimensional inversions were performed using the method described in Julia et al. [2000, 2003]. In this method, a linearized iterative algorithm is employed to invert for a one-dimensional layered model by minimizing a weighted least-squares norm consisting of one or more data sets, a model roughness norm, and a matrix of differences between inverted and preset model parameters. The method was developed to jointly invert receiver functions and surface wave dispersion curves. For this study, the influence factor for receiver functions was set to zero.

For checking how well the inversion results fit the data, synthetic dispersion curves were generated from the 1-D models, and then from these curves RMS misfits for the Rayleigh phase and group velocity measurements were computed (Figure 8). Average RMS misfits are ~0.051 km/sec and ~0.038 km/sec for group and phase velocity dispersion curves, respectively. RMS misfit values from group velocities for shorter periods (10 – 45 s) are slightly higher than misfits from longer periods (45 – 140 s), which might result from complexity in shallow (i.e., crustal) structure. The RMS misfits are within the range of the uncertainties of the 2-D phase velocity maps (~0.06 km/sec) obtained by the bootstrap resampling technique.

4.2 Results of one-dimensional inversion

After inverting for a 1-D velocity model for all 102 points in Figure 6, a quasi-three-dimensional shear wave velocity model was generated by taking the 1-D shear wave velocity profiles and at every 10 km depth interval interpolating between them using a minimum curvature gridding algorithm [*Smith and Wessel*, 1990]. Figure 9 shows depth slices and cross sections through the model. Structure below 200 km depth is not shown because structure below that depth is poorly resolved. The color scale is centered on a

velocity of 4.50 km/s (white), which is the average shear wave velocity in PREM over the depth interval from the Moho to 200 km.

Horizontal slices at 75 km and 100 km depths (Figures 9a and b) show a broad zone of low velocities beneath the entire Shield, with the lowest velocities (< 4.1 km/s) located beneath the southwestern part of the Shield and the MMN volcanic line. At deeper depths (Figures 9c-e), the low velocity regions become localized in a linear zone oriented in a SE-NW direction along the Red Sea coast and a NS direction beneath the MMN volcanic line.

Vertical slices through the model show velocity variations beneath the middle part of the Shield (A-A' in Figure 9f), the northern part of the Shield passing through the MMN volcanic line (B-B' in Figure 9g), and along the Red Sea coast (C-C' in Figure 9h). Profiles A-A' and B-B' show that the region with lower-than-average velocities is mainly confined above ~150 km depth under the Shield, and does not extend far to the east beneath the Platform. The lowest velocities are observed along the Red Sea coast and the low velocity region extends to at least 200 km depth (Figure 9h).

To illustrate further the regional differences in structure between parts of the Shield and the Platform, in Figure 9i we show one-dimensional velocity profiles from the southern part of the Shield (curve a), the MMN volcanic line (curve b), the eastern part of the Shield

(curve c), and the Platform (curve d). The one-dimensional velocity profile for the Platform (point d on Figure 9a) was obtained using Rayleigh wave phase velocities between 35 and 150 s from the Harvard model [*Ekstrom et al.*, 1997] and group velocities from 10 to 45 s from Pasyanos [2005]. For comparison, we also show the PREM model and a model for Proterozoic lithosphere in southern Africa (the Namaqua-Natal Belt (NNB) from Li and Burke [2006]). The NNB is used as a reference because it is the same age as the Neoproterozoic terrains that comprise the Arabian Shield.

In the Arabian Shield, the average shear velocity in the mantle to a depth of ~150 km is ~ 4.2 km/s, or ~0.3 km/s lower than in the PREM model and ~0.5 km/s lower than in the NNB. The velocity profile for the southern part of the Shield (profile a in Figure 9i) shows lower velocities than in any other place above 100 km depth, with the lowest velocity (~ 4.0 km/s) occurring at 90 km depth. The velocity profile for the MMN volcanic line (profile b in Figure 9i) is similar to velocities from the southern part of the Shield below 100 km depth. The velocity profile from the Platform (profile d in Figure 9i) shows higher velocities than PREM between the Moho and ~100 km depth, and PREM-like velocities below 100 km depth (profile d in Figure 9i).

Dispersion curves from points a-c in Figure 9a are shown in Figure 10, and for comparison, the dispersion curves from the Harvard group [*Ekstrom et al.*, 1997] for the same locations are also plotted. Dispersion curves from the MMN volcanic line and the border between the Arabian Shield and Platform area (points b and c in Figure 9a) are not that different from dispersion curves from the Harvard group, but the dispersion curve from the southern part of the Arabian Shield (point a in Figure 9) shows lower phase velocities with increasing period.

5.0 Discussion

The main features in the quasi-three-dimensional velocity model are 1) a broad low velocity region extending to a depth of ~150 km everywhere beneath the Shield, and 2) a low velocity structure localized along the Red Sea coast and MMN volcanic line at depths > ~150 km. Velocities below 150 km depth along the Red Sea coast and MMN volcanic line are approximately 7% lower than the average velocity in PREM in the same depth range. A similar low velocity structure at depths > ~150 km was also imaged by Park et al. [2007] by inverting body wave travel time residuals. In this section, we investigate the implications of these features for understanding the geodynamic origin of the upper mantle

thermal anomaly, and consequently the cause of the Cenozoic uplift and volcanism on the Shield.

We begin by examining the temperature structure of the thermally perturbed upper mantle under the Shield lithosphere and lithospheric thickness. Faul and Jackson [2005] found that the derivative of the shear wave velocity in the upper mantle depends mainly on grain size and temperature perturbation, and they obtained a temperature derivative of ~1.2 m/s/K at an average temperature of 1280 °C for a 10 mm grain size. Using a temperature derivative of 1.2 m/s/K and the observed velocity perturbation in our model of 0.3-0.5 km/s described in the previous section, a temperature reduction of ~250 - 330 K is obtained for the upper mantle under the Shield. This temperature reduction is possibly sufficient to produce partial melting related to the Cenozoic volcanism found on the Shield [*Gazzaz and Hashad*, 1991; *Gettings*, 1982; *Jackson et al.*, 2002; *Karato*, 1993; *Sato et al.*, 1988].

To estimate the thickness of the lithosphere, we follow the reasoning presented in Weeraratne et al. [2003] and use the depth of the maximum velocity gradient (negative gradient) to define the base of the lithosphere. Figure 11 shows the depth of the maximum negative gradient obtained from our velocity model for profiles A-A' and B-B'. The base of the lithosphere is ~90-100 km beneath most of the southern part of the Shield. In the

northern part of the Shield under the MMN volcanic line, the thinnest lithosphere is observed (~ 70 km thick), increasing in thickness to ~ 100 km near the Platform boundary (Figure 11b). Both profiles show the thinnest lithosphere near the Red Sea coast. Hansen et al. [2007] recently estimated lithospheric thickness beneath the Shield using S-wave receiver functions. They reported thin (~50 km) lithosphere under the Red Sea thickening toward the Arabian Platform, where it is ~ 110-120 km thick. The results from Hansen et al. [2007] are shown for comparison in Figure 11, and there is strong agreement between the two studies.

What are the implications of the thin, hot Shield lithosphere for uplift across the Arabian Peninsula? The average elevations of the Arabian Shield and Platform are ~1200 and ~700 m, respectively [*Bohannon et al.*, 1989; *Camp and Roobol*, 1992]. If we consider only the temperature variation in the lithosphere between the Shield and Platform, then the density variation in the lithosphere can be obtained from $d\rho = -\rho\alpha_v dT$ [*Turcotte and Schubert*, 2001], where α_v is the thermal coefficient of expansion ($\sim 3.2 \times 10^{-5} / K$). Using an estimated temperature variation (dT = 250 – 330 K) and a lithospheric mantle density of ρ = 3.26 g/cm^3, we obtain a density reduction for the lithospheric mantle beneath the Arabian Shield of 0.034 – 0.026 g/cm^3. The amount of isostatic uplift resulting from this

density reduction is 0.32 – 0.56 km, roughly consistent with the observed difference in the mean elevations of the Shield and Platform. Much higher elevations, for example up to 3 km in some parts of the Asir Province, are observed along the Red Sea coast. These regions of higher elevation probably result from a combination of lithosphere thinning and dynamic uplift, as discussed by Hansen et al. [2007] and Daradich et al. [2003], and not just from heating of the lithospheric mantle.

In order to interpret the thermal anomaly observed at both lithospheric and sublithospheric mantle depths vis-à-vis a geodynamic process, we need to consider the results from several other relevant studies.

1) As noted in section 2.0, receiver function studies of the 410 and 660 km discontinuities report little evidence for thermally perturbed mantle transition zone structure beneath the Shield [*Benoit et al.*, 2003; *Kumar et al.*, 2002]. However, Benoit et al. [2006] found that the 660 km discontinuity beneath Ethiopia is elevated, indicating that there could be a thermal connection between the anomalous lower and upper mantle structure under Ethiopia.

2) Daradich et al. [2003] and Hansen et al. [2007] have suggested that dynamic uplift induced by large-scale mantle flow associated with the African superplume has led to

rift-flank uplift adjacent to the Red Sea and a broad topographic tilt to the entire Arabian plate.

3) Evidence for sublithospheric mantle flow under the Shield in a generally northward direction has been provided by Tkalčić et al [2006] using a joint inversion of receiver function and surface wave dispersion measurements, and by Hansen et al. [2006] using SKS splitting measurements. Tkalčić et al. [2006] found strong S-wave polarization anisotropy (~ 10%), such that V_{SV} is faster than V_{SH} in the southwestern part of the Shield, and vice versa in the northwestern part of the Shield. Hansen et al. [2006] found N-S fast polarization directions for SKS waves.

4) A number of tomographic models, for example the models from Ritsema et al. [1999], Debayle et al. [2001], Grand [2002], Montelli et al. [2006], and Simmons et al. [2007], show a low velocity region under Afar/Ethiopia, possibly originating from the lower mantle anomaly commonly referred to as the African Superplume, which rise to shallow upper mantle depths under the Arabian Shield.

5) Many previous studies have suggested mantle plume models for the origin of the Cenozoic uplift and volcanism on the Arabian Shield. Burke [1996] suggested that plumes exist in many places beneath the African and Arabian plates related with topographic swells

and volcanism. Camp and Roobol [1992] suggested the existence of a narrow deep rooted mantle upwelling beneath the MMN volcanic line and a second one to the south beneath Afar. In contrast to multi-plume models, a single plume upwelling beneath Afar and lateral flow along the Red Sea coast was suggested by Ebinger and Sleep [1998]. The multi- and single plume models were examined by Park et al. [2007] using body wave tomography models, and they concluded that their models were consistent with either the single plume model [*Ebinger and Sleep*, 1998], or a superplume model.

Considering the results of these previous studies, along with our new velocity model (Figure 9), we offer the interpretation illustrated in Figure 12 to explain the origin of the thermally perturbed upper mantle under the Arabian Shield. The model invokes a thermal upwelling originating in the lower mantle that rises through the transition zone under Ethiopia and Afar (i.e., the African Superplume). In the upper mantle the warm mantle material flows to the north and northwest under the eastern margin of the Red Sea and under the Shield lithosphere. The flow of this warm mantle rock is preferentially channeled by pre-existing thinned lithosphere along the Red Sea coast [*Ebinger and Sleep*, 1998], thus creating a deeper low velocity zone (i.e., ≥ 150 km) under that part of the Shield. The warm mantle rock heats the Shield lithosphere and leads to Cenozoic volcanism on the surface, as

it migrates northwards. The generally northward flow of warm mantle rock is reflected in the N-S orientation of the fast polarization direction of SKS splitting [*Hansen et al.*, 2006].

This interpretation is consist with the model of Park et al. [2007], as well as with continental-scale and global tomographic images [e.g., *Debayle et al.*, 2001; *Grand*, 2002; *Montelli et al.*, 2006; *Ritsema et al.*, 1999; *Simmons et al.*, 2007; *Zhao*, 2001] showing a broad low velocity zone in the upper mantle under the Shield. We further suggest that the general northward flow of warm mantle material may extend to the north beyond the Shield, where post 12-Ma volcanism is found in Syria, Jordan, and northern Saudi Arabia, along with elevated topography (Figure 1).

6.0 Summary

A model of upper mantle structure beneath the Arabian Shield obtained from Rayleigh wave phase velocity tomography shows a broad low velocity region in the lithospheric mantle across the Shield and a low velocity region at depths ≥ 150 km localized along the Red Sea coast and MMN volcanic line. The velocity reduction in the upper mantle corresponds to a temperature anomaly of ~250 – 330 K. The estimated thickness of the lithosphere from the model is ~90-100 km beneath the southern part of the

Shield, ~70 km beneath the northern Shield under the MMN volcanic line, and ~100 km near the Platform boundary.

These finding, in particular the region of continuous low velocities along the Red Sea and MMN volcanic line, do not support interpretations for the origin of the Cenozoic plateau uplift and volcanism on the Shield invoking two separate plumes. When combined with images of the 410 and 660 km discontinuities beneath the southern part of the Arabian Shield [*Benoit et al.*, 2003; *Kumar et al.*, 2002], body wave tomographic models [*Park et al.*, 2007], a S-wave polarization analysis [*Tkalčić et al.*, 2006], and SKS splitting results [*Hansen et al.*, 2006], our new model supports an interpretation invoking a thermal upwelling of warm mantle rock originating in the lower mantle under Africa that crosses through the transition zone beneath Ethiopia and moves to the north and northwest under the eastern margin of the Red Sea and the Arabian Shield. In this interpretation, the difference in mean elevation between the Platform and Shield can be attributed to isostatic uplift caused by heating of the lithospheric mantle under the Shield, with significantly higher region along the Red Sea possibly resulting from a combination of lithosphere thinning and dynamic uplift.

Acknowledgments

We thank Charles J. Ammon for use of his LSQR 2-D inversion code for mapping phase velocities. This work has been supported by the National Science Foundation (grants EAR 993093, 0003424, and 0505812) and the Department of Energy (contract DE-FC52-05NA26602). Prepared by LLNL under Contract DE-AC52-07NA27344.

References

Al-Amri, M., and A. Al-Amri (1999), Configuration of the seimolographic networks in Saudi Arabia, *Seismological Research Letters*, *70*, 322-331.

Al-Damegh, K., et al. (2004), Regional seismic wave propagation (Lg and Sn) and Pn attenuation in the Arabian Plate and surrounding regions, *Geophysical Journal International*, *157*, 775-795.

Al-Damegh, K., et al. (2005), Crustal structure of the Arabian Plate; new constraints from the analysis of teleseismic receiver functions, *Earth and Planetary Science Letters*, *231*, 177-196.

Al-Lazki, A. I., et al. (2004), Pn tomographic imaging of mantle lid velocity and anisotropy at the junction of the Arabian, Eurasian and African plates, *Geophysical Journal International*, *158*, 1024-1040, ISI:000223470400019.

Almond, D. C. (1986), The relation of Mesozoic-Cainozoic volcanism to tectonics in the Afro-Arabian Dome, *Journal of Volcanology and Geothermal Research*, *28*, 225-246.

Bassin, C., et al. (2000), The current limits of resolution for surface wave tomography in North America, *Eos, Transactions, American Geophysical Union*, *81*, 897.

Benoit, M. H., et al. (2006), Mantle transition zone structure and upper mantle S velocity variations beneath Ethiopia: Evidence for a broad deep-seated thermal anomaly, *Geochem. Geophys. Geosyst.*, *7*, Q11013, doi:10.1029/2006GC001398.

Benoit, M. H., et al. (2003), Upper mantle P wave velocity structure and transition zone thickness beneath the Arabian Shield, *Geophysical Research Letters*, *30*, ISI:000183302200002.

Berhe, S. M. (1997), The Arabian-Nubian Shield, *Oxford Monographs on Geology and Geophysics*, *35*, 761-771.

Bohannon, R. G. (1989), Style of extensional tectonism during rifting, Red Sea and Gulf of Aden, *Journal of African Earth Sciences*, *8*, 589-602.

Bohannon, R. G., et al. (1989), The timing of uplift, volcanism, and rifting peripheral to the Red Sea; a case for passive rifting?, *Journal of Geophysical Research, B, Solid Earth and Planets*, *94*, 1683-1701.

Burke, K. (1996), The African Plate, *S. Afr. J. Geol.*, *99*, 341-409, ISI:A1996WD18000001.

Camp, V. E., and M. J. Roobol (1989), The Arabian continental alkali basalt province; Part I, Evolution of Harrat Rahat, Kingdom of Saudi Arabia; with Suppl. Data 89-04, *Geological Society of America Bulletin*, *101*, 71-95.

Camp, V. E., and M. J. Roobol (1992), Upwelling Asthenosphere Beneath Western Arabia And Its Regional Implications, *Journal Of Geophysical Research-Solid Earth*, *97*, 15255-15271, ISI:A1992JR87500012.

Camp, V. E., et al. (1991), Tomographic and volcanic asymmetry around the Red Sea; constraints on rift models; discussion and reply [modified], *Tectonics*, *10*, 649-656.

Capaldi, G., et al. (1987), Tertiary anorogenic granites of the western border of the Yemen Plateau, *Lithos*, *20*, 433-444.

Civetta, L., et al. (1978), K-Ar ages of the Yemen Plateau, *Journal of Volcanology and Geothermal Research*, *4*, 307-314.

Coleman, R. G., and A. V. McGuire (1988), Magma Systems Related To The Red-Sea Opening, *Tectonophysics*, *150*, 77-100, ISI:A1988P640700005.

Daradich, A., et al. (2003), Mantle flow, dynamic topography, and rift-flank uplift of Arabia, *Geology*, *31*, 901-904, ISI:000185692200018.

Debayle, E., et al. (2001), Seismic evidence for a deeply rooted low-velocity anomaly in the upper mantle beneath the northeastern Afro/Arabian continent, *Earth And Planetary Science Letters*, *193*, 423-436, ISI:000172954200013.

du Bray, E. A., et al. (1991), Age and petrology of the Tertiary As Sarat volcanic field, southwestern Saudi Arabia, *Tectonophysics*, *198*, 155-180.

Dziewonski, A., et al. (1969), A technique for the analysis of transient seismic signals, *Bulletin of the Seismological Society of America*, *59*, 427-444.

Dziewonski, A. M., et al. (1981), Preliminary Reference Earth Model (Prem), *Eos, Transactions, American Geophysical Union*, *62*, 332.

Ebinger, C. J., and N. H. Sleep (1998), Cenozoic magmatism throughout east Africa resulting from impact of a single plume, *Nature*, *395*, 788-791, ISI:000076607400053.

Ekstrom, G., et al. (1997), Measurements and global models of surface wave propagation, *Journal of Geophysical Research*, *102*, 8137-8157.

Faul, U. H., and I. Jackson (2005), The seismological signature of temperature and grain size variations in the upper mantle, *Earth and Planetary Science Letters*, *234*, 119-134, ISI:000229693200009.

Gazzaz, M. A., and A. H. Hashad (1991), Radiogenic heat production and heat flow in the northern Arabian Shield, *Journal of African Earth Sciences*, *13*, 323-332.

Gettings, M. E. (1982), Heat-flow measurements at shot point along the 1978 Saudi Arabian Seismic Deep-Refaction LINE, Part 2: Discussion and Interpretation, *U.S. Geological Survey, Open-File*, *Report 82-794*.

Gettings, M. E., and Anonymous (1981), A heat flow profile across the Arabian Shield and Red Sea, *Eos, Transactions, American Geophysical Union*, *62*, 407.

Grand, S. P. (2002), Mantle shear-wave tomography and the fate of subducted slabs, *Philosophical Transactions - Royal Society. Mathematical, Physical and Engineering Sciences*, *360*, 2475-2491.

Hansen, S., et al. (2007), Imaging Ruptured Lithosphere beneath the Red Sea and Arabian Peninsula, *Earth and Planetary Science Letters*, *259*, 256-265.

Hansen, S., et al. (2006), Combined Plate Motion and Density Driven Flow in the Asthenosphere beneath Saudi Arabia: Evidence from Shear-wave Splitting and Seismic Anisotropy, *Geology*, *34*, 869-892.

Jackson, I., et al. (2002), Grain-size-sensitive seismic wave attenuation in polycrystalline olivine, *J. Geophys. Res.-Solid Earth*, *107*, ISI:000181225600001.

Julia, J., et al. (2003), Lithospheric structure of the Arabian Shield from the joint inversion of receiver functions and surface-wave group velocities, *Tectonophysics*, *371*, 1-21, ISI:000184855600001.

Julia, J., et al. (2000), Joint inversion of receiver function and surface wave dispersion observations, *Geophysical Journal International*, *143*, 99-112.

Karato, S. (1993), Importance Of Anelasticity In The Interpretation Of Seismic Tomography, *Geophysical Research Letters*, *20*, 1623-1626, ISI:A1993LT38700026.

Knox, R. P., et al. (1998), Upper mantle S velocities beneath Afar and western Saudi Arabia from Rayleigh wave dispersion, *Geophysical Research Letters*, *25*, 4233-4236, ISI:000077019300033.

Kumar, M. R., et al. (2002), Crustal structure and upper mantle stratigraphy of the Arabian shield, *Geophysical Research Letters*, *29*, 1242, ISI:000178886800038.

Lawrence, J. F., et al. (2006), Rayleigh wave phase velocity analysis of the Ross Sea, Transantarctic Mountains, and East Antarctica from a temporary seismograph array, *Journal Of Geophysical Research-Solid Earth*, *111*, ISI:000238572500001.

Li, A. B., and K. Burke (2006), Upper mantle structure of southern Africa from Rayleigh wave tomography, *J. Geophys. Res.-Solid Earth*, *111*, ISI:000241300000001.

Maggi, A., and K. Priestley (2005), Surface waveform tomography of the Turkish-Iranian Plateau, *Geophysical Journal International*, *160*, 1068-1080.

Martinez, F., and J. R. Cochran (1988), Structure and tectonics of the northern Red Sea; catching a continental margin between rifting and drifting, *Tectonophysics*, *150*, 1-32.

McGuire, A. V. (1988), The mantle beneath the Red Sea margin; xenoliths from western Saudi Arabia, *Tectonophysics*, *150*, 101-119.

McGuire, A. V., and R. G. Bohannon (1989), Timing of mantle upwelling; evidence for a passive origin for the Red Sea Rift, *Journal of Geophysical Research, B, Solid Earth and Planets*, *94*, 1677-1682.

Mellors, R. J., et al. (1999), Regional waveform propagation in the Arabian Peninsula, *Journal Of Geophysical Research-Solid Earth*, *104*, 20221-20235, ISI:000082473500015.

Menke, W., and V. Levin (2002), Anomalous seaward dip of the lithosphere-asthenosphere boundary beneath northeastern USA detected using differential-array measurements of Rayleigh waves, *Geophysical Journal International*, *149*, 413-421, ISI:000175441300012.

Mohr, P. (1983), Ethiopian flood basalt province, *Nature*, *303*, 577-584.

Mohr, P. A., et al. (1988), The Ethiopian flood basalt province, in *Continental Flood Basalts*, edited by J. D. Macdougal, pp. 65-110, Kluwer Academic, Boston, Mass.

Montelli, R., et al. (2006), A catalogue of deep mantle plumes: New results from finite-frequency tomography, *Geochemistry Geophysics Geosystems*, *7*, ISI:000241982600001.

Mooney, W. D., et al. (1985), Saudi Arabian seismic-refraction profile: A traveltime interpretation of crustal and upper mantle structure, *Tectonophysics*, *111*, 173-246.

Nyblade, A. A., and C. A. Langston (2002), Broadband seismic experiments probe the East African rift, *EOS Trans. AGU*, *83*, 405-408.

Paige, C. C., and M. A. Saunders (1982), LSQR: An Algorithm for Sparse Linear Equations and Sparse Least Squares, *ACM Trans. Math. Softw.*, *8*, 43-71.

Pallister, J. S. (1987), Magmatic history of Red Sea rifting; perspective from the central Saudi Arabian coastal plain; with Suppl. Data 87-11, *Geological Society of America Bulletin*, *98*, 400-417.

Park, Y., et al. (2007), Upper mantle structure beneath the Arabian Peninsula and Northern Red Sea from teleseismic body wave tomography: Implications for the origin of

Cenozoic uplift and volcanism in the Arabian Shield, *Geochem. Geophys. Geosyst.*, *8*, doi:10.1029/2006GC001566.

Pasyanos, M. E. (2005), A variable resolution surface wave dispersion study of Eurasia, North Africa, and surrounding regions, *Journal Of Geophysical Research-Solid Earth*, *110*, ISI:000234249800004.

Pasyanos, M. E., and W. R. Walter (2002), Crust and upper-mantle structure of North Africa, Europe and the Middle East from inversion of surface waves, *Geophysical Journal International*, *149*, 463-481.

Ritsema, J., et al. (1999), Complex shear wave velocity structure imaged beneath Africa and Iceland, *Science*, *286*, 1925-1928, ISI:000084003400042.

Rodgers, A. J., et al. (1999), Lithospheric structure of the Arabian Shield and Platform from complete regional waveform modelling and surface wave group velocities, *Geophysical Journal International*, *138*, 871-878, ISI:000082541900021.

Sandvol, E., et al. (2001), Tomographic imaging of Lg and Sn propagation in the Middle East, *Pure Appl. Geophys.*, *158*, 1121-1163, ISI:000170476700003.

Sato, H., et al. (1988), Thermal Structure Of The Low Velocity Zone Derived From Laboratory And Seismic Investigations, *Geophysical Research Letters*, *15*, 1227-1230, ISI:A1988Q473200014.

Sebai, A., et al. (1991), $^{40}Ar/^{39}Ar$ dating of alkaline and tholeiitic magmatism of Saudi Arabia related to the early Red Sea rifting, *Earth and Planetary Science Letters*, *104*, 473-487.

Shim, J. P. (1989), *Numerical Recipes - the Art of Scientific Computing - Press,Wh, Flannery,Bp, Teukolsky,Sa, Vetterling,Wt*, 107-108 pp.

Simmons, N. A., et al. (2007), Thermochemical structure and dynamics of the African superplume, *Geophys. Res. Lett.*, *34*, ISI:000243848800004.

Smith, W. H. F., and P. Wessel (1990), Gridding with continuous curvature splines in tension, *Geophysics*, *55*, 293-305.

Tkalčić, H., et al. (2006), A multistep approach for joint modeling of surface wave dispersion and teleseismic receiver functions: Implications for lithospheric structure of the Arabian Peninsula, *Journal of Geophysical Research*, *111*, doi:10.1029/2005JB004130.

Turcotte, D. L., and G. Schubert (2001), *Geodynamics, Application of Continuum Physics to Geological Problem*, Cambridge Univ. Press, New York.

Vernon, F., et al. (1996), Observations from regional and teleseismic earthquakes recorded by a deployment of broadband seismometers in the Saudi Arabian Shield, *EOS Trans. AGU*, *77*, 478.

Villaseñor, A., et al. (2001), Shear velocity structure of central Eurasia from inversion of surface wave velocities, *Physics of the Earth and Planetary Interiors*, *123*, 169-184.

Weeraratne, D. S., et al. (2003), Evidence for an upper mantle plume beneath the Tanzanian Craton from Rayleigh wave tomography, *Journal of Geophysical Research, B, Solid Earth and Planets*, *108*, no.9, 17, 2005-014343.

Wolfe, C. J., et al. (1999), Shear-wave splitting across western Saudi Arabia: The pattern of upper mantle anisotropy at a Proterozoic shield, *Geophysical Research Letters*, *26*, 779-782, ISI:000079207400039.

Zeyen, H., et al. (1997), Styles of continental rifting: crust-mantle detachment and mantle plumes, *Tectonophysics*, *278*, 329-352, ISI:A1997YE13100019.

Zhao, D. (2001), Seismic structure and origin of hotspots and mantle plumes, *Earth And Planetary Science Letters*, *192*, 251-265, ISI:000171914500001.

Figure 1. Map of the study area showing topography, seismic station locations and major tectonic features. Broadband seismic stations of the SANDSN and the 2000-2002 Ethiopia PASSCAL Broadband Seismic Experiment are denoted by white and black triangles, respectively. The 1995-1997 PASSCAL Broadband Seismic Experiment stations are represented by green squares, and the IRIS/GEOSCOPE broadband station locations are shown as bold circles. The red hatch pattern shows post 12 Ma volcanic fields. The outline of the Arabian Shield is shown with the black dashed line.

Figure 2. The distribution of earthquakes used for Rayleigh wave phase velocity measurements. The red solid lines show major plate boundaries.

Figure 3. Ray path coverage maps for periods of 52, 80, 100, and 140 s. Broadband seismic stations of the SANDSN and the 2000-2002 Ethiopia PASSCAL Broadband Seismic Experiment are denoted by red triangles and black circles, respectively. The 1995-1997 PASSCAL Broadband Seismic Experiment stations are represented by black squares. Numbers on the right edge on each map indicate the number of ray paths for each period.

Figure 4. An example trade-off curve between final travel-time reduction and model roughness at 75 s. The selected optimum smoothing parameter is shown with the big red circle.

Figure 5. Synthetic checkerboard resolution tests for periods of 52, 80, 100, and 140 s. Gray lines indicate outlines of 300 × 300 km input checkers consisting of ±10% velocity anomalies. Black polygon indicates the region where our model has the best resolution.

Figure 6. Phase velocity variations at periods of 52, 80, 100, and 140 s. Areas with limited resolutions are shown with faded colors. The black dots on each map represent locations used for extracting phase velocity dispersion curves to invert for one-dimensional velocity models. Numbers on the right edge on each map show the mean velocity (in km/s) obtained from the final iteration of the inversion for each period. The white polygon endoses the area with the best resolution.

Figure 7. Maps showing Moho depth from (a) receiver functions [*Al-Damegh, et al.*, 2005; *Kumar, et al.*, 2002] and seismic refraction profiles [*Mooney, et al.*, 1985] (dashed line with red stars in Figure 7a) and (b) the CRUST2.0 model [*Bassin, et al.*, 2000]. Numbers in Figure 7a indicate the Moho depth reported from receiver function studies for each station.

Figure 8. RMS misfits maps for (a) Rayleigh wave group, (b) phase velocity, and (c) average misfits of Rayleigh wave group and phase velocity dispersion curves from theoretical values using a one-dimensional inversion for each point on Figure 6.

Figure 9. Quasi-three-dimensional shear wave velocity model obtained by compiling the one-dimensional models for each point (see text for further explanation). Horizontal slices (a-e) through the model are shown for depths of 75, 100, 150, 180, and 200 km. Vertical cross sections (f-h) are shown with exaggerated topography shown in grey for three profiles (A-A', B-B', and C-C'). Locations for the profiles are given in Figure 8a. (i) One-dimensional shear wave velocity profiles for the Arabian Shield (points a-d in Figure 9a), Platform (point d in Figure 9a), the Namaqua-Natal Belt in South Africa (red solid line) [*Li and Burke*, 2006], and the PREM model (blue solid line) [*Dziewonski, et al.*, 1981].

Figure 10. Examples of Rayleigh wave phase velocity dispersion obtained from two-dimensional velocity maps (Figures 6 and 8). The locations of points a, b, and c are shown on Figure 9. For comparison, Rayleigh wave phase velocity dispersion curves for the same locations from the Harvard model [Ekstrom et al., 1997] are plotted with dashed lines.

Figure 11. Estimated lithosphere thickness from our model (blue diamonds), together with Moho depths and lithosphere thickness from Hansen et al. [2007] (solid lines with red circles), superimposed on the vertical depth profiles (a) A-A' and (b) B-B' shown in Figure 9. Topography is shown in grey. Vertical lines on topography indicate the boundary between the Arabian Shield and Platform. Numbers on Figure 11a show the density (g/cm^3) used for calculating isostatic uplift.

Figure 12. A sketch of block diagram showing our prefered interpretation for the upper mantle thermal anomaly under the Arabian Shield. Anomalously warm mantle rock (orange and red areas) flows from the lower mantle into the upper mantle beneath Ethiopia, and then continues to move in north and northwest directions in the upper mantle beneath the Shield, giving rise to a N-S fast polarization direction for SKS waves, thinning of the llithosphere along the Red Sea Coast, heating of the Shield lithosphere, and uplift and volcanism on the Shield.

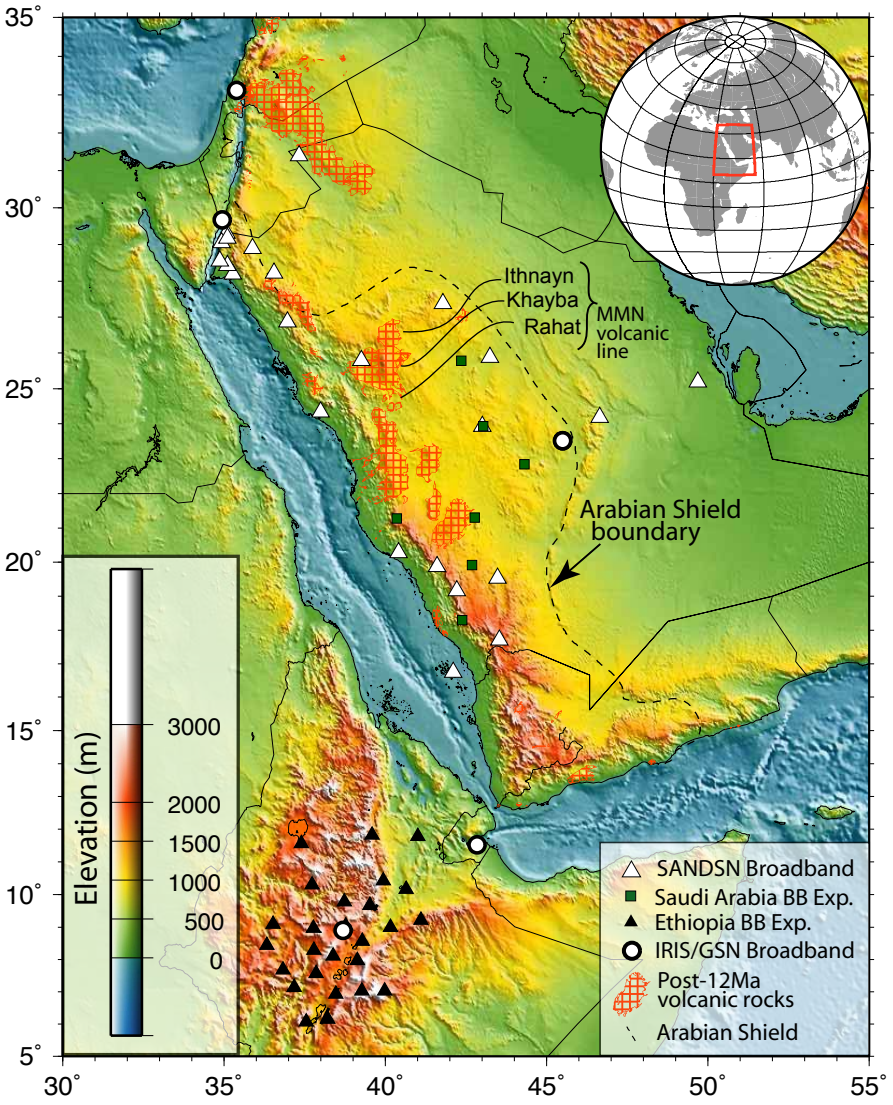
35˚
30˚
25˚
20˚
15˚
10˚
5˚
30˚
35˚
40˚
45˚
50˚
55˚
Ithnayn
Khayba
Rahat
MMN volcanic line
Arabian Shield boundary
Elevation (m)
3000
2000
1500
1000
500
0
SANDSN Broadband
Saudi Arabia BB Exp.
Ethiopia BB Exp.
IRIS/GSN Broadband
Post-12Ma volcanic rocks
Arabian Shield

Figure 1.

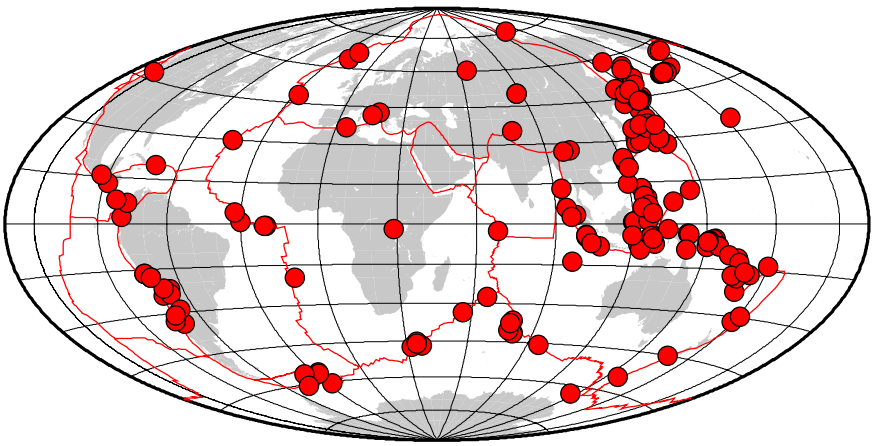

Ray paths at 52 s

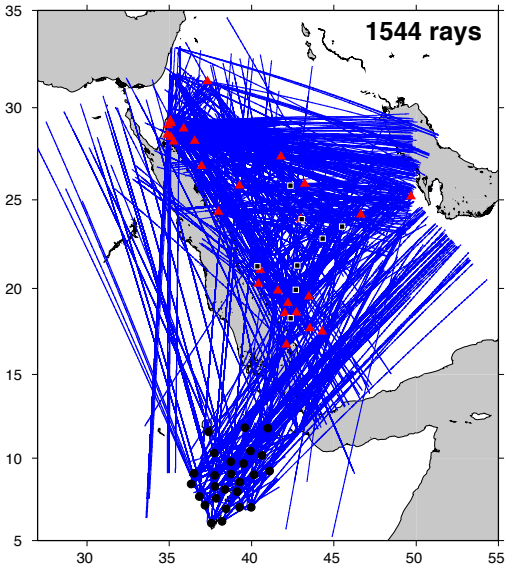

Ray paths at 80 s

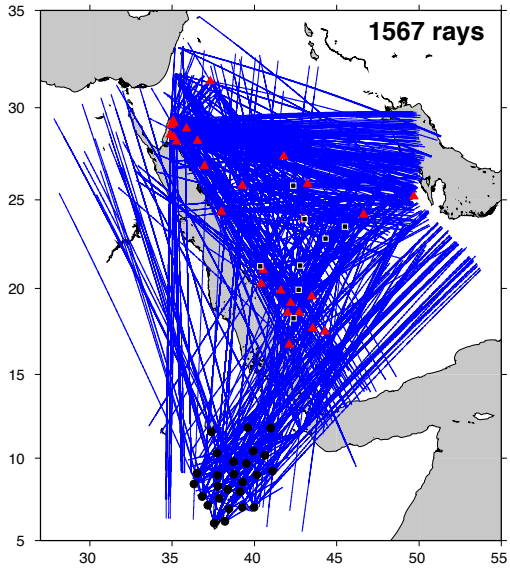

Ray paths at 100 s

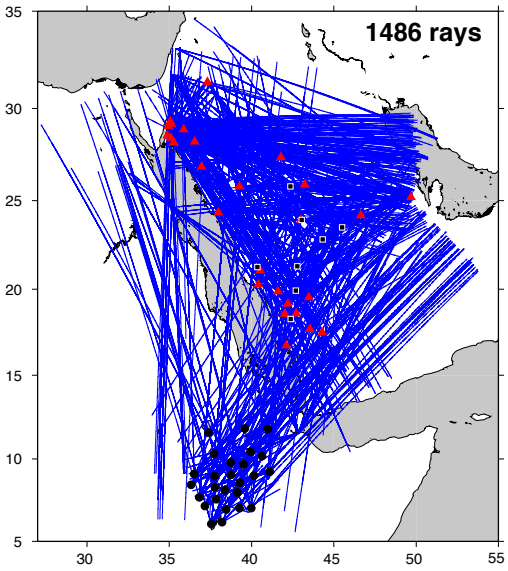

Ray paths at 140 s

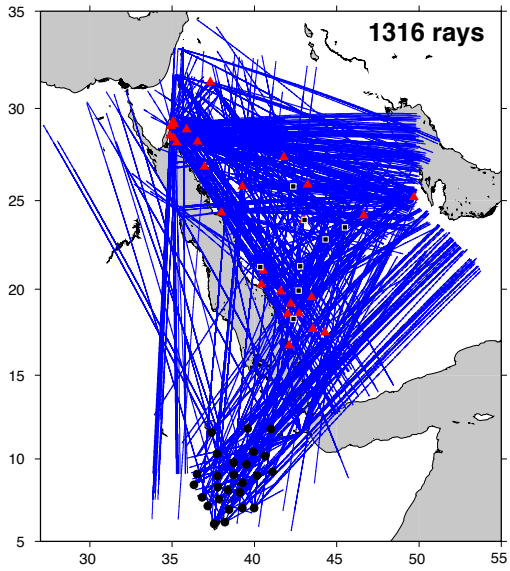

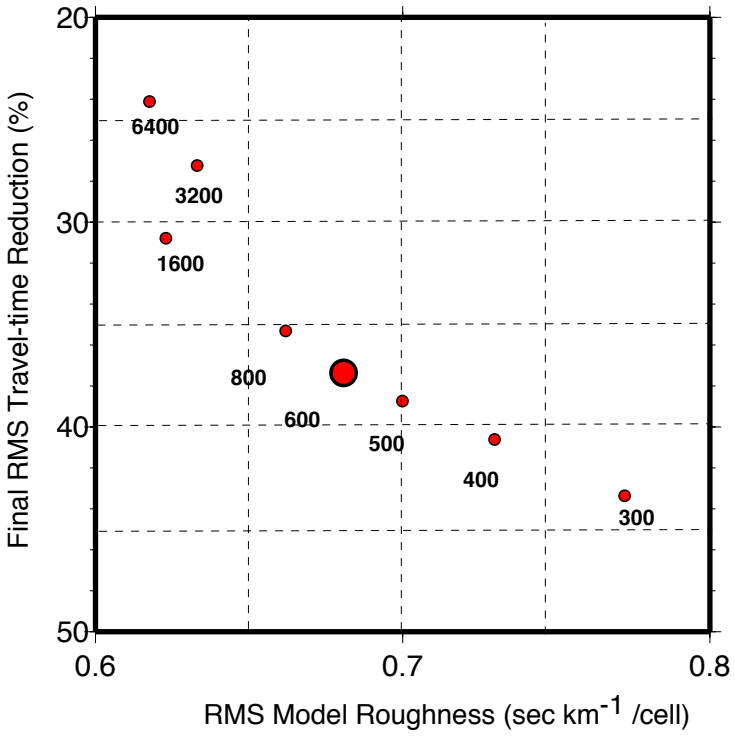
20
30
40
50
0.6
0.7
0.8
Final RMS Travel-time Reduction (%)
RMS Model Roughness (sec km-1 /cell)
6400
3200
1600
800
600
500
400
300

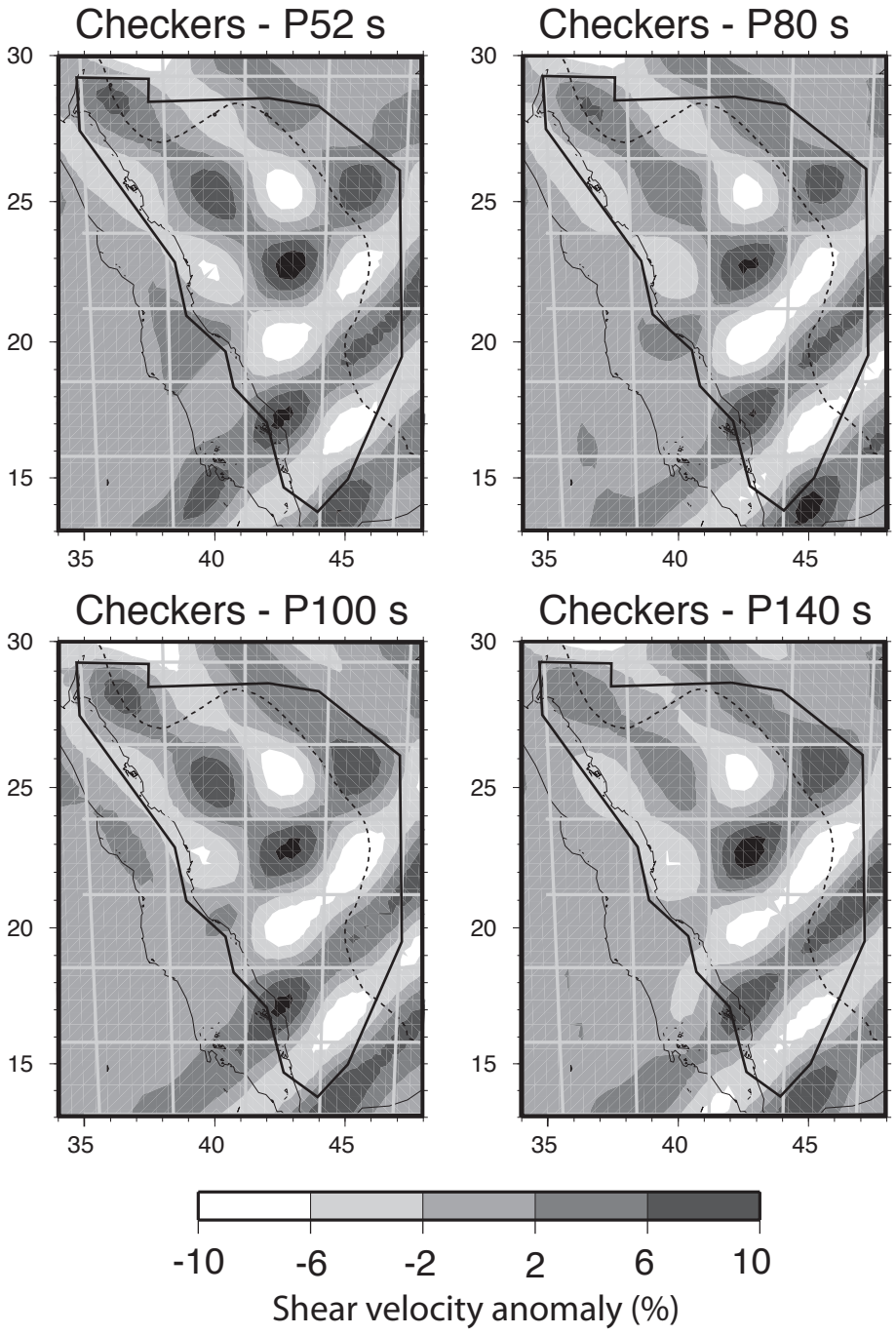
Checkers - P52 s
Checkers - P80 s
Checkers - P100 s
Checkers - P140 s
30
25
20
15
35
40
45
-10
-6
-2
2
6
10
Shear velocity anomaly (%)

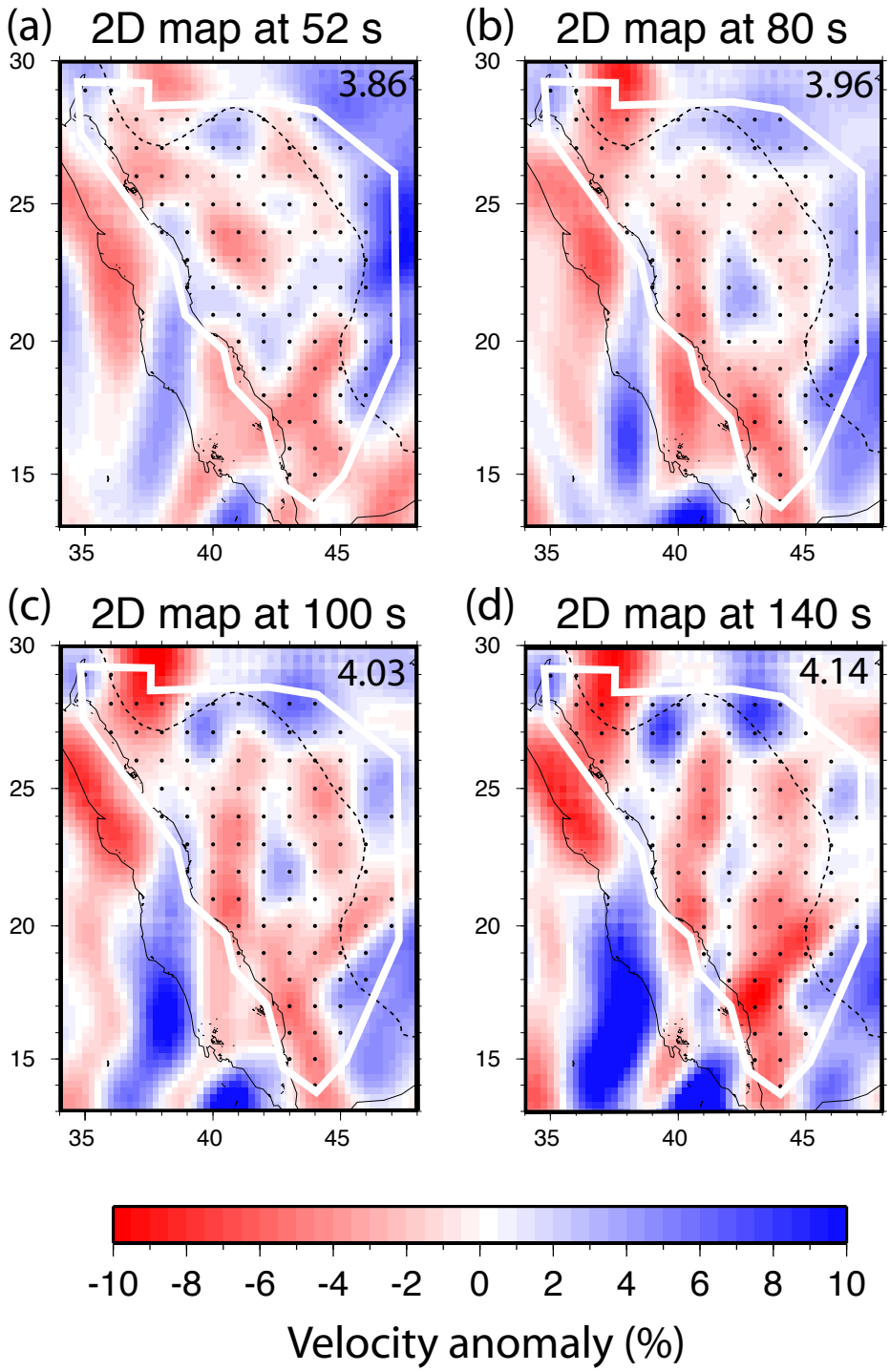
(a) 2D map at 52 s
3.86
(b) 2D map at 80 s
3.96
(c) 2D map at 100 s
4.03
(d) 2D map at 140 s
4.14
30
25
20
15
35
40
45
-10 -8 -6 -4 -2 0 2 4 6 8 10
Velocity anomaly (%)

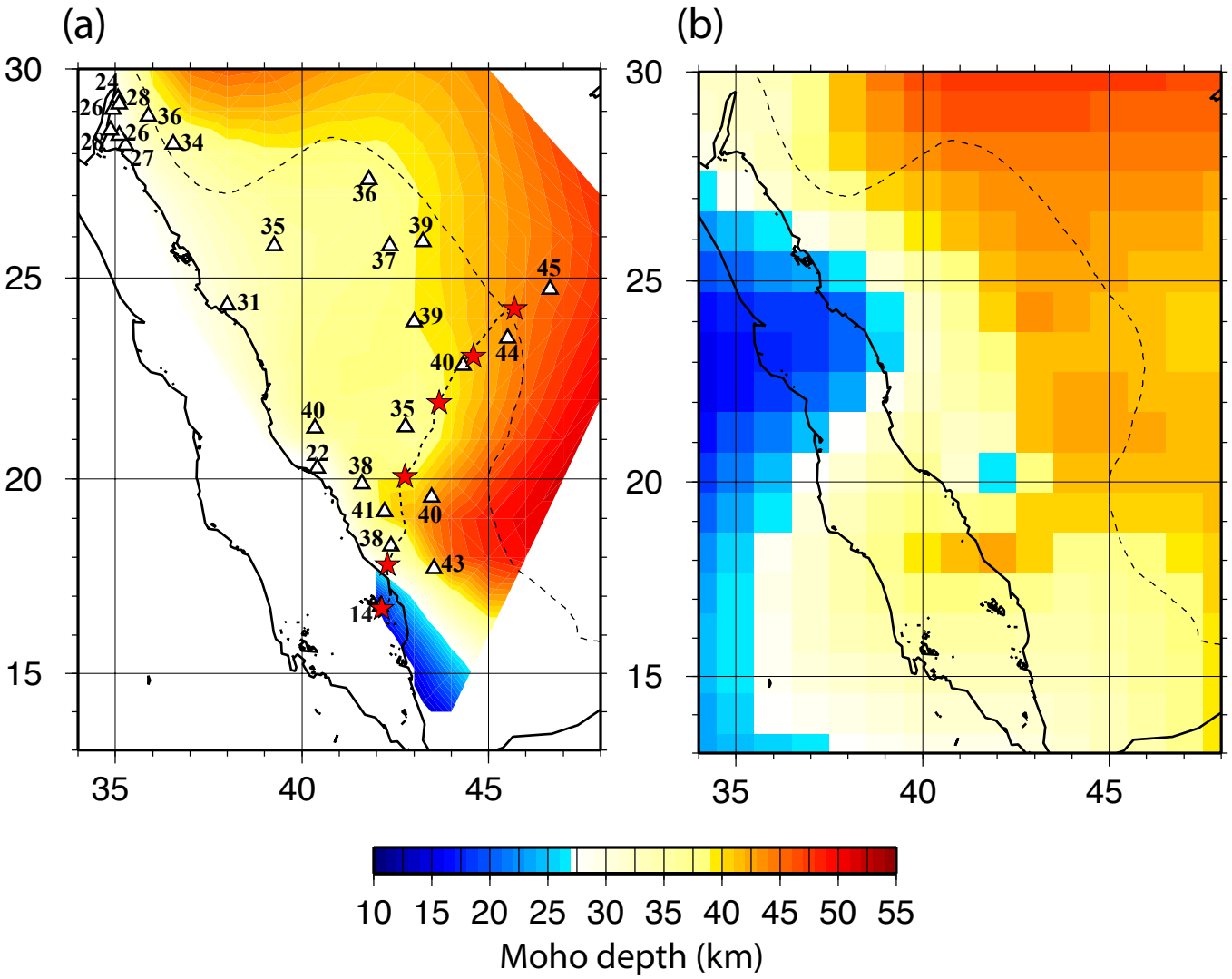
(a)
(b)
30
25
20
15
35
40
45
24
28
26
36
26
34
27
36
35
39
37
45
31
39
44
40
40
35
22
38
41
40
38
43
14
10 15 20 25 30 35 40 45 50 55
Moho depth (km)

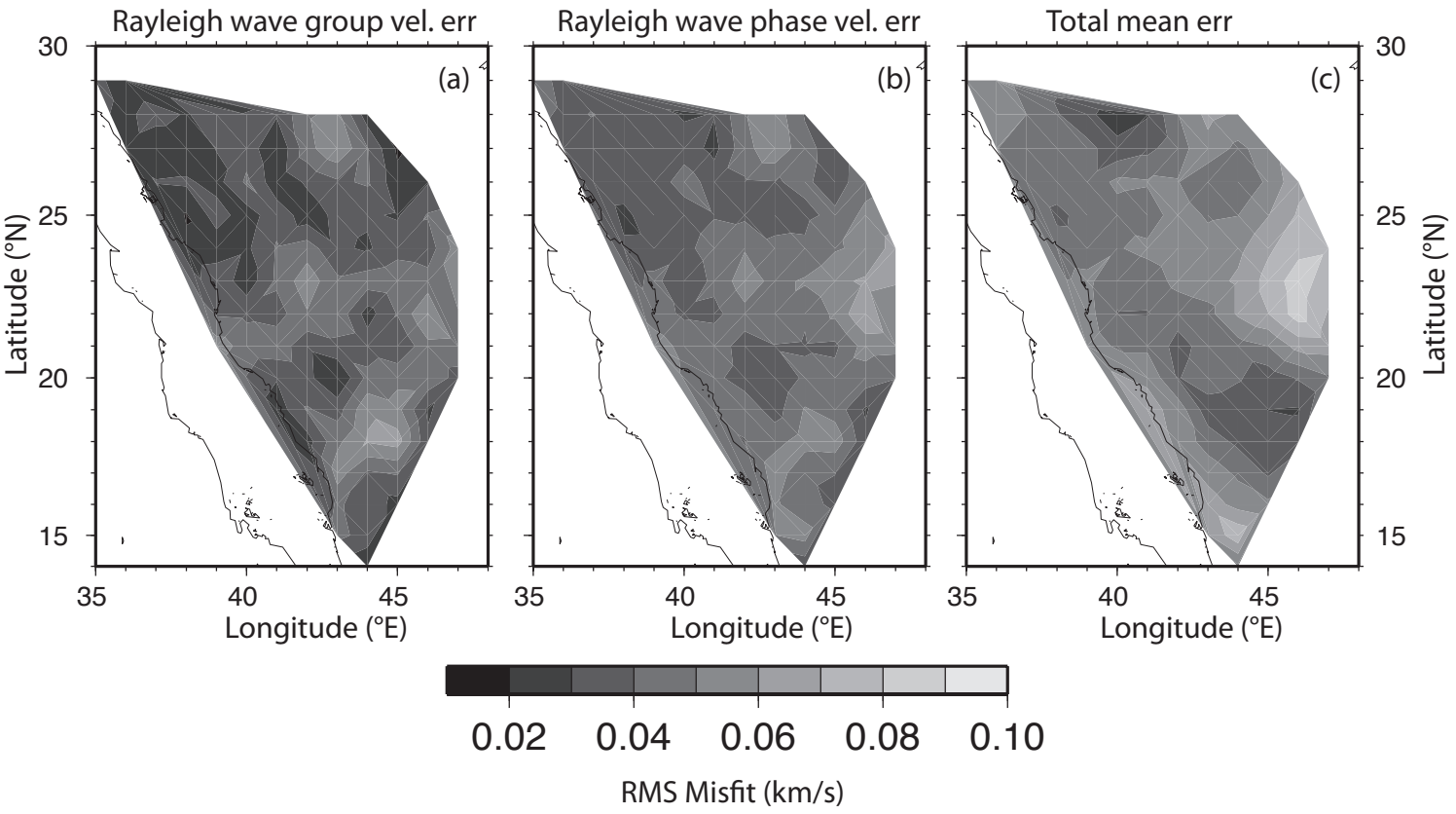
Rayleigh wave group vel. err
Rayleigh wave phase vel. err
Total mean err
(a)
(b)
(c)
30
25
20
15
Latitude (°N)
35
40
45
Longitude (°E)
0.02
0.04
0.06
0.08
0.10
RMS Misfit (km/s)

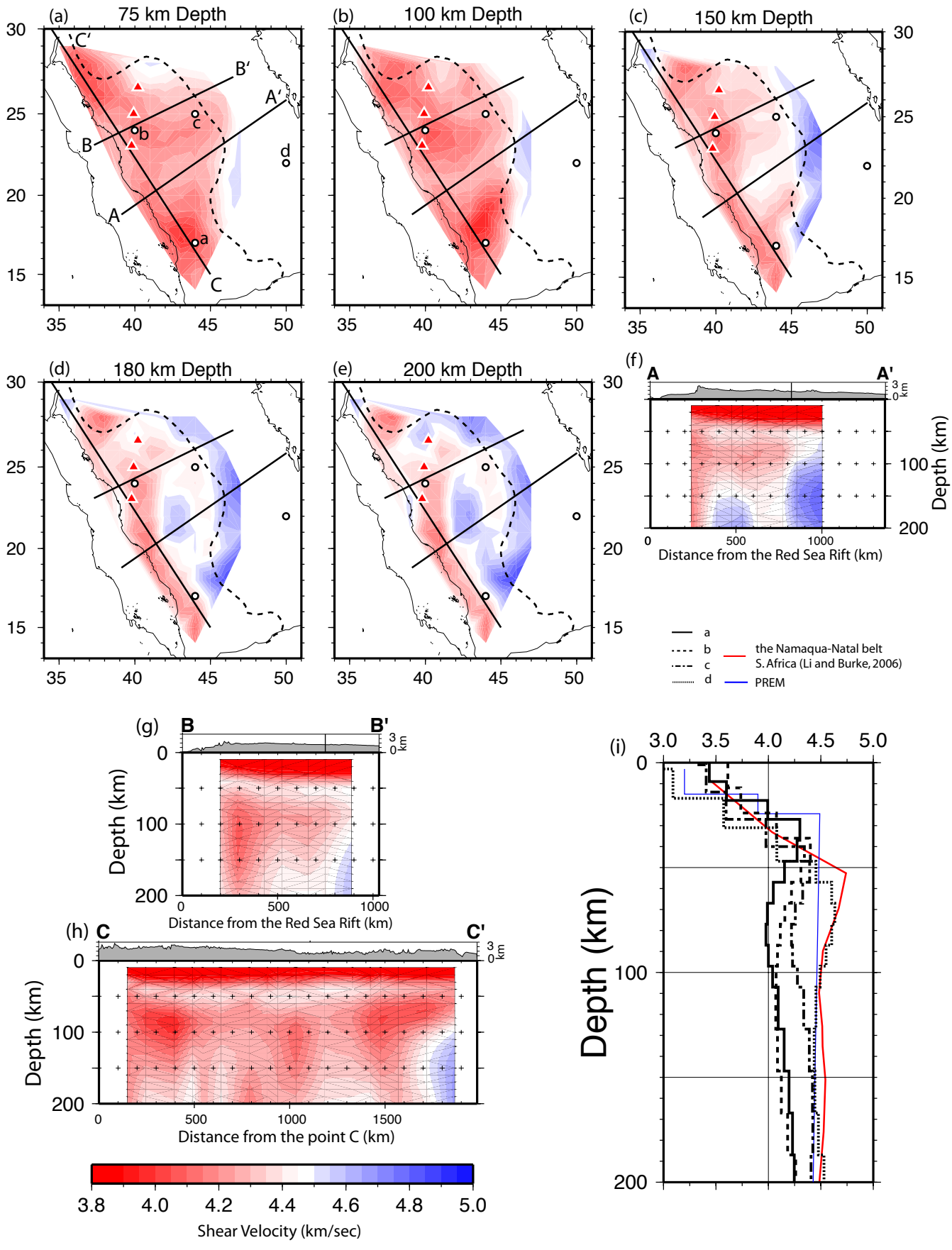
(a) 75 km Depth
(b) 100 km Depth
(c) 150 km Depth
(d) 180 km Depth
(e) 200 km Depth
(f)
(g)
(h)
(i)
A
A'
B
B'
C
C'
a
b
c
d
Depth (km)
Distance from the Red Sea Rift (km)
Distance from the point C (km)
Shear Velocity (km/sec)
the Namaqua-Natal belt
S. Africa (Li and Burke, 2006)
PREM

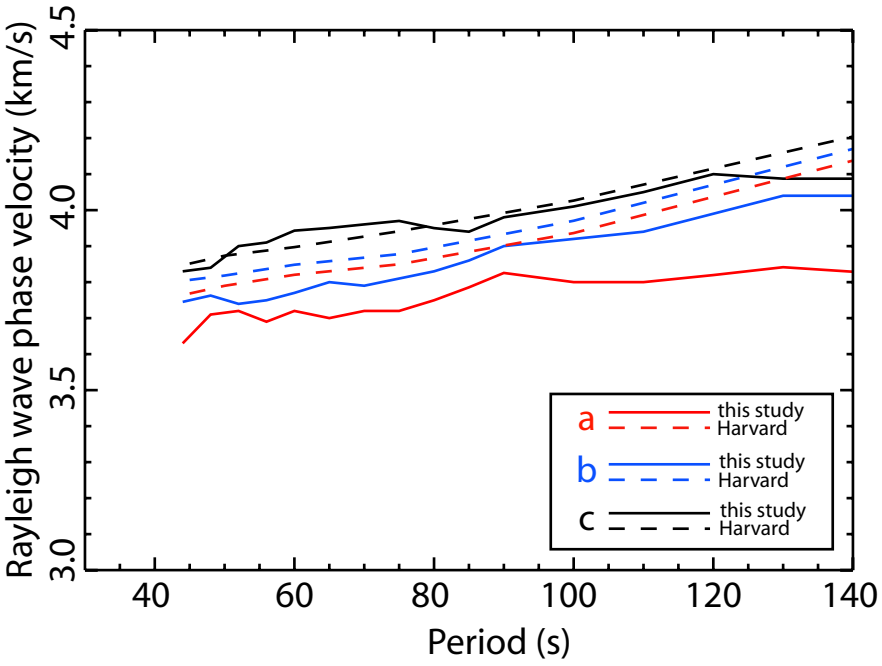
Rayleigh wave phase velocity (km/s)
3.0
3.5
4.0
4.5
40
60
80
100
120
140
Period (s)
a
this study
Harvard
b
this study
Harvard
c
this study
Harvard

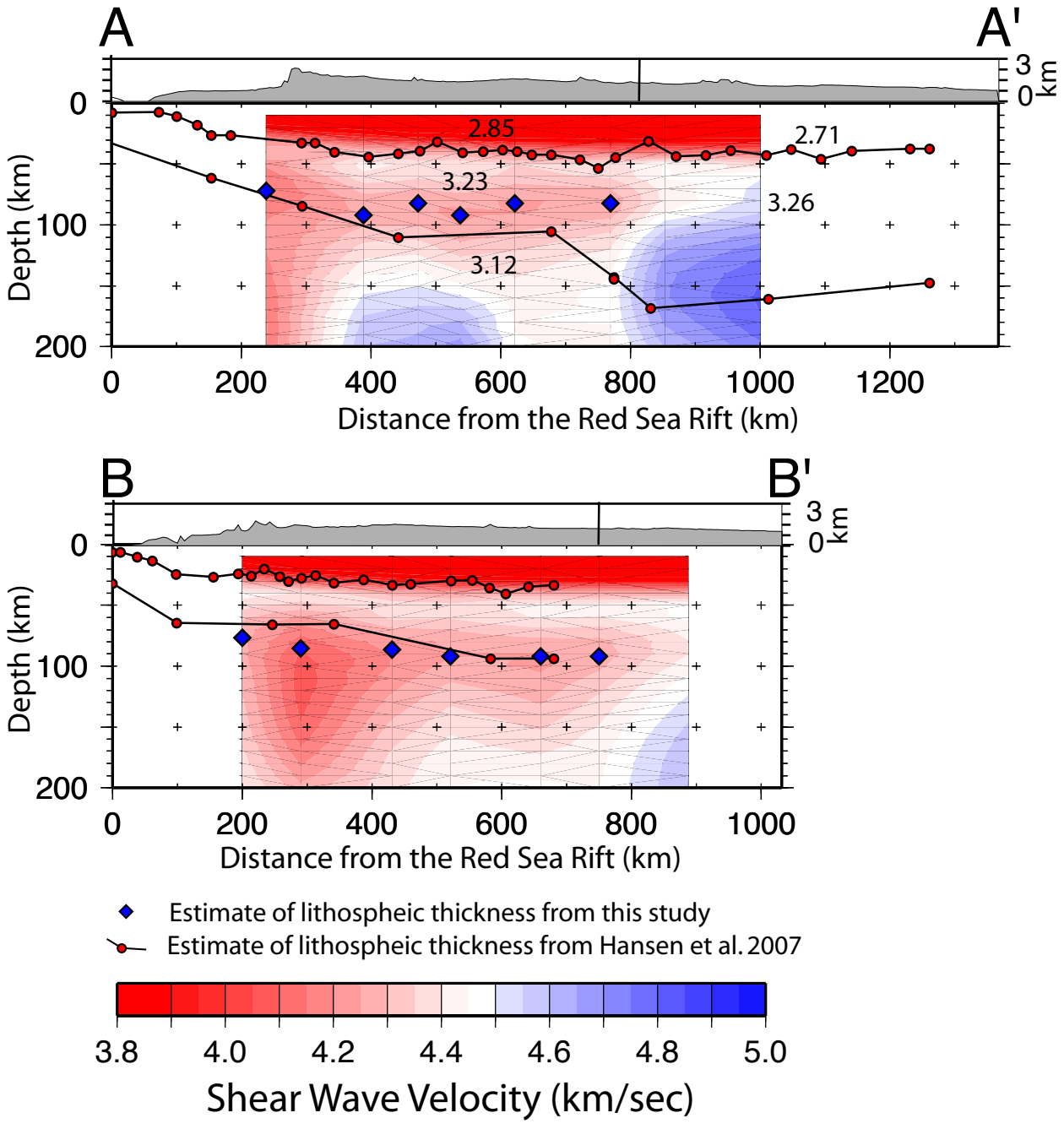
A
A'
3
0
km
0
100
200
Depth (km)
2.85
2.71
3.23
3.26
3.12
0
200
400
600
800
1000
1200
Distance from the Red Sea Rift (km)
B
B'
3
0
km
0
100
200
Depth (km)
0
200
400
600
800
1000
Distance from the Red Sea Rift (km)
Estimate of lithospheic thickness from this study
Estimate of lithospheic thickness from Hansen et al. 2007
3.8
4.0
4.2
4.4
4.6
4.8
5.0
Shear Wave Velocity (km/sec)

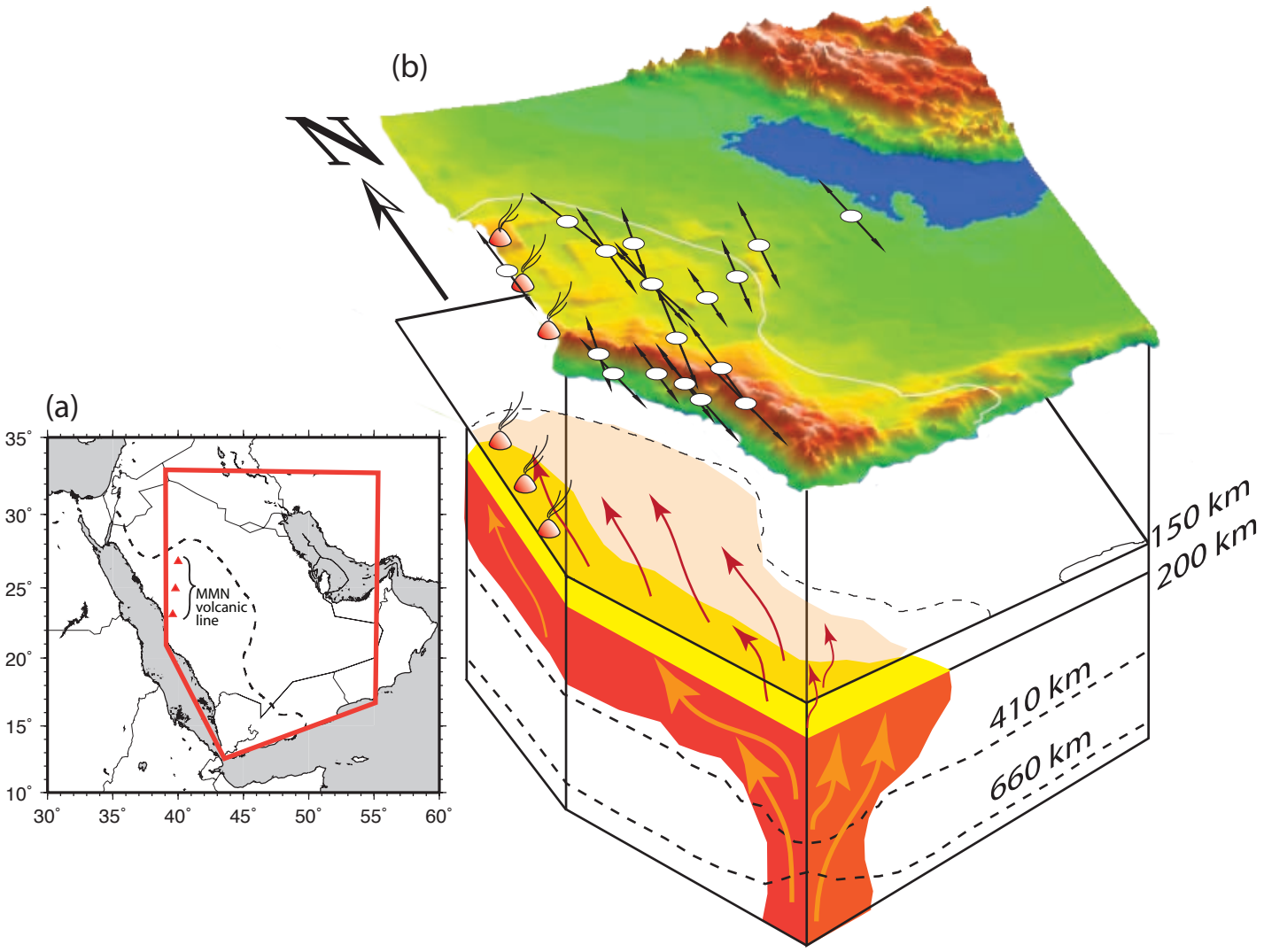
(a)
35°
30°
25°
20°
15°
10°
30°
35°
40°
45°
50°
55°
60°
MMN
volcanic
line
(b)
N
150 km
200 km
410 km
660 km